In-situ estimation of erosion model parameters using an advection-diffusion model and Bayesian inversion

W. C. Edge[1], **M. D. Rayson**[1], **N. L. Jones**[1], **G. N. Ivey**[1]

[1]Oceans Graduate School and Oceans Institute, University of Western Australia, Perth, Western Australia, Australia

Key Points:

- Probabilistic framework to estimate unobserved erosion model parameters using sparse measurements collected above the seabed.
- General approach can be updated with any model parameterization and quantitatively compared.
- The framework is applicable to many similar data sets with both unsteady or quasi-steady forcing and response.

Corresponding author: W. C. Edge, william.edge@research.uwa.edu.au

Abstract

We describe a framework for the simultaneous estimation of model parameters in a partial differential equation using sparse observations. Monte Carlo Markov Chain (MCMC) sampling is used in a Bayesian framework to estimate posterior probability distributions for each parameter. We describe the necessary components of this approach and its broad potential for application in models of unsteady processes. The framework is applied to three case studies, of increasing complexity, from the field of cohesive sediment transport. We demonstrate that the framework can be used to recover posterior distributions for all parameters of interest and the results agree well with independent estimates (where available). We also demonstrate how the framework can be used to compare different model parameterizations and provide information on the covariance between model parameters.

Plain Language Summary

We describe a framework for the simultaneous estimation of multiple unobserved parameters by combining observations of a tracer with a numerical model. This framework uses Bayesian inference techniques established in statistical literature to estimate the unobserved parameters of interest used in the model with uncertainty quantification. We explain the key components of this framework in simple terms to encourage its use for analysing other unsteady processes and performing quantitative inference on parameters that are difficult or impossible to measure directly. We then demonstrate the framework's efficacy by applying it to three case studies from the field of cohesive sediment transport that all use the transport equation (advection-diffusion). Inferred parameter values show good agreement with independent estimates, where available.

1 Introduction

Numerical solutions to partial differential equations (PDE) are a key tool in modelling complex processes. There is, however, often a natural variation of the key parameters required for accurate modelling which presents a challenge in many fields of research (e.g. boundary layer physics (Souza et al., 2020), pulmonary circulation (Păun et al., 2018), groundwater flow (Ghouili et al., 2017), population spread (Soubeyrand & Roques, 2014), and sediment transport (Manning & Schoellhamer, 2013; Valipour et al., 2017). Measurements can provide insight into these complex processes, but in many cases the parameter of interest is difficult to observe directly (e.g. Liñán Baena et al., 2009; Egan et al., 2021; Maa & Kwon, 2007; Mattsson et al., 2016; Smyth et al., 2021). Furthermore, the unsteady time- and space-dependent nature of some processes can mean that methods developed under controlled settings (e.g. steady forcing in a laboratory) are not readily implementable in real world examples.

To overcome this challenge, we describe a framework to estimate PDE parameters by combining time- and space-dependent observations with a numerical model of a known PDE to solve the so-called inverse problem. The typical approach when solving the inverse problem is to determine the set of model parameters, θ, that minimises the residual, ϵ, between the observations and model outcome. For a time-dependent, 1-dimensional spatial model this is then written

$$C_{obs}(z,t) = f(z,t;\theta) + \epsilon, \tag{1}$$

which states that the observations, $C_{obs}(z,t)$ (herein C), can be represented by a chosen model, $f(z,t;\theta)$, plus the residual, ϵ. We have used z to represent the spatial dimension and t to represent time. Here we employ a probabilistic framework based on Bayesian inference to solve the inverse problem (described in Section 2). This allows for the simultaneous estimation of probability distributions for all model parameters and the resid-

ual ϵ, thus providing full uncertainty quantification and parameter covariance information.

When modelling environmental processes the required parameters may take a range of probable values, i.e., a probabilistic description of the parameters is often most suitable. Quantifying this range provides more meaningful insights than maximum likelihood estimation alone, especially when the parameter probability distribution is non-Gaussian or multi-modal. Bayesian frameworks for solving inverse problems with uncertainty quantification have been described extensively in the statistical literature, but uptake by researchers in many fields has been slow. For this reason, we take a pedagogical approach when describing the method used in this study. The Bayesian inference framework can be employed for parameter estimation in a wide range of numerical model applications that use a known (but potentially complex) state equation that is computationally inexpensive to solve.

To demonstrate this method we examine a numerical model of the one-dimensional unsteady advection-diffusion equation (ADE), widely used to model tracer evolution in fluid flows. This type of process has intrinsic variability and measurements of tracer concentration can be noisy. In addition, typical numerical models of the ADE may be idealised, as in this work, and boundary or initial conditions may also contain errors or require estimation with sub-models. These sub-models may also be idealised or mis-specified, and can include additional unknown parameters that contribute uncertainty. This makes a numerical model of the ADE a good example for simultaneous parameter estimation with uncertainty quantification.

We test this methodology on three different case studies of increasing complexity, all from the field of cohesive sediment transport. This field is a suitable test for the methodology used herein because there are a number of parameters that cannot be directly observed. Recent research in this field continues to identify large differences in all key parameter estimates depending on site, time, and/or method (see Maa and Kwon (2007) for an example of particle settling velocity, Valipour et al. (2017) for critical bed strength, and Egan et al. (2021) for the erosion rate parameter). Similar physics-driven approaches to parameter estimation using observations have been performed before in cohesive sediment environments (e.g. Brand et al., 2015; Zhang et al., 2021), but not using a Bayesian framework. Schmelter et al. (2011) assessed bed load transport sediment transport in a Bayesian framework and provide an excellent summary of the key fundamentals for Bayesian modelling. Before analysing the case studies we first describe the Bayesian framework used for parameter estimation in more detail. Then we describe the numerical model used for the case studies, along with two boundary flux (sub-)models implemented within the numerical model. Following that we describe the observations, model specifics, and results of the inference for each case study.

The three case studies are similar in nature so they use the same numerical model, which limits the repetition of model specifics that are incidental to the general methodology. Case Study 1 is from an annular flume erosion experiment conducted in Baltimore Harbour by Maa et al. (1998) (digitised from Sanford and Maa (2001), Figure 1b). Case Study 2 is a synthetic data set generated from the numerical model itself, with the inputs designed to mimic typical unsteady tidal forcing. Case Study 3 is an application of the method to a set of complex (unsteady and noisy) real-world observations from Edge et al. (2021). Our goal is to use these case studies of sediment transport to gradually introduce complexity and demonstrate the efficacy of the method for estimating un-observable, yet important, parameters used in the prediction of the response of a geophysical system.

2 Parameter inference methods

2.1 General approach

We first describe the general framework used in this study to solve the inverse problem posed in Equation 1. Bayesian statistical and computational techniques are used to simultaneously estimate the posterior probability of the model parameters (θ), given some observations C, stated $p(\theta|C)$. The approach is derived from Bayes' theorem,

$$p(\theta|C) \propto p(C|\theta)p(C). \tag{2}$$

The posterior probability density (herein the posterior) is proportional to the product of the likelihood, $p(C|\theta)$, and the prior probability density, $p(C)$. The prior and posterior are m-dimensional distributions, where m is the number of parameters to sample. The likelihood is a cost function that evaluates the chosen model and penalises model outcomes that are further from the observations. Only the likelihood function is maximised in a frequentist approach; there is no incorporation of prior beliefs in that framework. One advantage of the Bayesian approach is that the prior on each parameter can represent information that is already known or expected, such as a plausible range of reported values from literature.

Note that in Equation 2 the parameter vector θ includes σ, which represents the standard deviation of ϵ, the residual from Equation 1. For this work we have assumed that the distribution of values in ϵ is homoskedastic (invariant with respect to predictor variables) and Gaussian, i.e. $\epsilon = \mathcal{N}(0, \sigma)$. Differences between the model outcome and the observations may be the result of natural variation, measurement error, or model mis-specification, all of which are encapsulated in σ. By estimating the magnitude of σ, Bayesian inference is able to partition these sources of uncertainty from the uncertainty in the parameter estimates. This allows for better parameter estimates while still accurately predicting the plausible range C may take.

The use of Markov Chain Monte Carlo (MCMC) sampling techniques allow the posterior to be approximated in the proportional form in Equation 2. For each step in a Markov Chain a new θ is proposed and Equation 2 is evaluated. By doing this, MCMC sampling is able to explore the posterior space and move towards regions of proportionally higher probability until a stationary distribution is found. The specifics of defining priors, computing the likelihood function, and sampling the posterior using MCMC sampling are described in more detail below.

2.2 Likelihood

The likelihood function quantifies the probability that θ was used to generate a set of observations, C. This allows us to compare the probability of different proposals for θ. At this point we separate θ into the model parameters, θ_{mod} and σ for clarity. The likelihood is assumed to be a Gaussian distribution for a sample of observations, $\mathbf{C} = (C_i, ..., C_n)$. For computational reasons the likelihood function is evaluated in log-space and can be written as

$$\mathcal{L}(y|\theta_{mod}, \sigma) = -\frac{n}{2}\ln(2\pi) - n\ln(\sigma) - \frac{1}{2\sigma}\sum_{i=1}^{n}\left(C_i - y_i\right)^2. \tag{3}$$

Here $y = f(\theta_{mod})$ is the output from our chosen model and n is the number of observations. Note that each element in θ_{mod} and σ are free parameters estimated during MCMC sampling.

2.3 Priors

The prior distributions on each parameter form the second component to the right-hand-side of Equation 2. They represent the probability that we assign to each param-

eter before we have performed the inference. Priors can be informative, weakly informative, or non-informative (diffuse). If we already have detailed information on a parameter, say from well-established physical theory, literature, or independent measurements, we can use an informative prior to limit the space the posterior can move to. Conversely, for parameters that potentially could occupy a large range, we can set priors to be diffuse so that MCMC sampling can explore this range without being penalised.

Our aim when defining the prior distributions for this research was to limit the posterior sample space to a reasonable range of values that were supported by physical theory and literature. This increases the efficiency of MCMC sampling and reduces the time required for individual chains to converge on a stationary distribution (Tarantola, 2004). When the chosen model is a numerical model, priors can also be used to restrict the parameter space to regions of model stability. For example, an explicit advection-diffusion numerical model becomes unstable when the Courant number exceeds one, so any parameter that may cause this to occur must be restricted.

The specific priors used for each case study are described before the results. All the priors used in this study were either half-normal ($\mathcal{H}$) or log-normal ($\ln\mathcal{N}$) distributions. These were used because all of the parameters in our chosen model could not be negative, including σ. Parameters that could be zero were assigned half-normal priors, while parameters that could not be zero were assigned log-normal distributions. This study was focused on the development and testing of the described methodology. Priors were set to be weakly informative, based on a range of possible values determined from literature.

2.4 MCMC sampling and evaluation

With the likelihood and prior distribution functions defined we can now use Markov Chain Monte Carlo (MCMC) sampling to investigate the posterior. The aim of MCMC sampling is to explore the posterior space until the chain (or chains) converge on a stationary target distribution. For a thorough explanation of MCMC sampling methods the reader is referred to Gelman et al. (2013, Part III).

For this work we have used Differential Evolution MCMC sampling (DE-MC) (Ter Braak, 2006), though we note that the method is independent of the specific MCMC sampling method. DE-MC is a variation of the Metropolis algorithm and uses information from other chains to improve the sampling efficiency for all chains. The advantage of DE-MC is it's speed of convergence, particularly in high dimensional problems. A practical advantage of the DE-MC sampler is that it does not require the computation of gradients of the likelihood function with respect to the parameters. Note that the framework was implemented with a different MCMC method (Dynesty, described in Speagle (2020)) with equivalent results.

Evaluation of convergence between chains was performed using common tests described in Gelman et al. (2013). Specifically, we determined convergence was met when the $\widehat{R}$ statistic was less than 1.05 for each parameter and the auto-correlation for all chains had dropped to near zero. If satisfactory convergence of the chains was achieved the results were deemed suitable for analysis and prediction.

3 The numerical model

Here we describe the specific numerical model used in this study, f, noting that in theory any model may take its place. The numerical model is a finite difference discretisation of the 1-dimensional unsteady advection-diffusion equation (ADE). The ADE, described next, can be used to model the transport of any scalar, C, in fluid flows (among other applications). The model is applied to three case studies from the field of cohe-

sive sediment transport. In this field the fluxes of C at the boundary (sediment-water interface) of the ADE model are key drivers of changes in C and much research has been undertaken to determine the best parameterizations for this process. In this section, we describe the chosen sub-models, herein boundary flux models, that we have used and define the parameters of interest.

3.1 The advection-diffusion equation

The full three dimensional time-space dependent form of the ADE can be written as

$$\frac{\partial C}{\partial t} + \nabla.(\boldsymbol{u})C = \nabla.(\gamma \nabla C) + S, \tag{4}$$

where C is the tracer concentration, $\boldsymbol{u}$ is the three-dimensional velocity vector, γ is the diffusivity, and S is a source or sink term.

In order to simplify this equation to one dimension we have made several assumptions. The primary assumption is that the observed process can be adequately represented in a single (vertical) dimension. First, we have assumed that vertical turbulent diffusion, denoted γ_z, is the only important component in the diffusivity term. Second, we have assumed that the horizontal flux divergence components (in $\nabla.\boldsymbol{u}C$) are small and can be ignored. Last, we have assumed that the only source and sink terms come from the model bottom boundary. The two boundary flux models are: a source of sediment to the water column by erosion, E, and a loss of sediment from the water column by deposition, D. Both terms are only applied to the lowest grid cell. The one-dimensional-vertical (1Dv) equation used in this study is thus

$$\frac{\partial C}{\partial t} + \frac{\partial (w - w_s)C}{\partial z} = \frac{\partial}{\partial z}\left(\gamma_z \frac{\partial C}{\partial z}\right) + E - D. \tag{5}$$

Note that the tracer used for this study is sediment, which is negatively buoyant, and the tracer settling velocity, w_s, is a parameter of interest and is applied to the vertical direction only (herein defined as positive downward). For this study w_s is assumed to be independent of time, space, and C.

In order to utilise the ADE we discretised each of the terms using an implicit finite difference method (2nd-order centred-time centred-space). The model was forced with observations of vertical current velocity (w) and bottom friction velocity (u_*, used to estimate the time-dependent bed shear stress and profile of the vertical turbulent diffusivity γ_z). The output from the model can then be compared to observations of C. The parameters of interest that we want to estimate are w_s and any parameters required for the chosen boundary flux model (described next).

3.2 Boundary flux models

In sediment transport studies, the upward fluxes into the water column from erosion and the downward fluxes out of the water column to the bed from deposition are key processes that control the magnitude of C. Erosion and deposition have been the subject of considerable investigation over the past six decades and the optimal models to represent these processes are still the subject of ongoing research.

To demonstrate the method described in this study we compared two erosion models. Both erosion models translate a known bed stress, τ_{bed}, into a flux C that is added to the lowest grid cell as a source term. The deposition flux was simply calculated as the product of w_s and the concentration in the lowest grid cell, C_0. We note that the method described in this research could be used for comparison and parameter estimation with any erosion or deposition boundary flux models, or combinations thereof.

The first erosion model tested was a variation of the popular Ariathurai-Partheniades equation, given by

$$E = M(\tau_{bed} - \tau_{cr})^b \quad \text{where} \quad \tau_{cr} = \tau_{cr0} \tag{6}$$

(Ariathurai, 1974), shown here without the denominator. Here τ_{bed} is the bed shear stress, which is known, and τ_{cr0}, M, and b are the erosion model parameters to infer. Herein this boundary flux model is referred to as *E1*.

The second erosion model tested was another variation of the Ariathurai-Partheniades equation where the term τ_{cr} was allowed to vary in proportion to the total C in the numerical model, m_c,

$$E = M(\tau_{bed} - \tau_{cr}) \quad \text{where} \quad \tau_{cr} = \tau_{cr0} + \tau_m m_c^{\tau_b}. \tag{7}$$

For this erosion model M, τ_{cr0}, τ_m, and τ_b are the parameters to infer. This erosion model is an approximation of what is commonly referred to as depth-limited erosion. Accurate modelling of depth-limited erosion requires a multi-layer bed model (e.g. Sanford, 2008) which was beyond the scope of this study. We used available literature to set the prior distributions for the free parameters in each boundary flux model, discussed below, before presenting the case study results.

3.3 Forcing the numerical model

There are several quantities necessary to force the numerical model which need to be either measured or estimated before the model can be run. The main observation required is a time series of the bottom friction velocity, u_*, or the bed stress, τ_{bed}, which are related to each other by $\tau_{bed} = \rho u_*^2$, where ρ is a measured or assumed water density. For all examples τ_{bed} was the input into the erosion models. In addition, if fluid vertical velocities are important at the site of interest, they can be included in the model (as they have been in Case Study 3).

The eddy diffusivity profile, γ_z, was generated using a parabolic model for unstratified flow (Dyer & Soulsby, 1988),

$$\gamma_z = \kappa u_* z \left(1 - \frac{z}{B_h}\right). \tag{8}$$

In this model κ is the von Karman constant, z is the height above the bed, and B_h is the height of the diffusivity profile. Above the boundary layer the diffusivity was set to a constant value of 10^{-4} m^2 s^{-1}. A single point at the top edge of the boundary layer was smoothed (quadratic interpolation) to remove the discontinuous transition between the parabolic model and the area of constant diffusivity. The height B_h was either constant or time-dependent, depending on the case study. Note that any diffusivity profile could be used with this method. To demonstrate our method we have thus chosen a simple profile, but the implementation of more sophisticated diffusivity models is a possible focus for future research. Estimation of the diffusivity profiles is only required one time before inference is performed, so this would not significantly increase the computation time.

4 Case studies

4.1 Setting priors

All three case studies chosen for this work come from the field of cohesive sediment transport and as such, they all exhibit similar behaviour. For this work we used weakly informative priors determined from the literature and used any independent results for comparison. Because we used weakly informative priors we were able to specify the same priors for all three case studies [Table 1].

Table 1. Specified prior distributions for all case studies, including the 95% credible intervals (CI) and relevant references.

Parameter	Prior	95% CI	References
$w_s \times 10^{-3}$ m s^{-1}	$ln\mathcal{N}(0.5, 0.7)$	(0.50, 5.34)	Neville (1986), Cartwright et al. (2013), Voulgaris and Meyers (2004), Maa and Kwon (2007), Manning and Schoellhamer (2013)
$M \times 10^{-4}$ kg m^{-2} s^{-1} (Pa^{-b})*	$\mathcal{H}(20)$	(44.83)	Winterwerp and van Kesteren (2004), Maa et al. (1998), Egan et al. (2021)
$\tau_{cr0} \times 10^{-2}$ Pa	$\mathcal{H}(3)$	(6.72)	Egan et al. (2021), Maa et al. (1998), Edge et al. (2021)
b / τ_b	$ln\mathcal{N}(0.25, 0.5)$	(0.48, 3.42)	Egan et al. (2021), Brand et al. (2015)
τ_m Pa $m_c^{-\tau_b}$	$ln\mathcal{N}(0.5, 1.5)$	(0.09, 31.05)	Sanford and Maa (2001), Brand et al. (2015)
$\sigma \times 10^{-3}$ kg m^{-3}	$\mathcal{H}(3)$	(6.72)	-

*M units include the term Pa^{-b} for the boundary flux model $E1$ but not for $E2$.

All the priors were defined using distributions that could not be negative based on physical theory and literature. Each parameter was scaled to be (close to) order one for MCMC sampling. For parameters where the literature indicated that the underlying value may span many orders of magnitude, such as M and τ_m, we used initial (user specified) testing to narrow down the likely range, and then specified priors to cover a few orders of magnitude. Our initial uncertainty in these parameters was reflected by the large 95% credible intervals (CI) of the priors [Table 1]. We compare and discuss the priors in light of the inferred posteriors in the case study results below.

4.2 Case Study 1: annular flume data

4.2.1 Observations

This case study is based on an annular flume experiment conducted in Baltimore Harbour (described in Maa et al., 1998). Note the data was digitised from the corrected results of total mass eroded (m_c) and bed shear stress (τ_{bed}) shown in Sanford and Maa (2001), Figure 1b, with m_c related to the depth-averaged tracer concentration ($\overline{C}$) by the height of the flume. This case study is typical of controlled erosion experiments performed over naturally deposited cohesive sediment beds. It involved a series of stepped increases to the applied bed stress and regular measurement of $\overline{C}$ over time [Figure 1]. In such tests the next step is typically initiated once $\overline{C}$ stabilises ($\partial\overline{C}/\partial t$ reaches zero). The relationship between bed strength (τ_c) and mass eroded (m_c) can then be examined by using the steady state values at the end of each step.

Here, the inference on the model parameters is performed using the entire time series of data, not just the steady points at the end of each bed stress step. Note that because this case study only uses the depth-averaged tracer concentration, $\overline{C}$, the advection-diffusion model is superfluous and the problem may be simplified to a boundary condition (as demonstrated by Zhang et al., 2021). Later case studies use spatially sparse observations of C. For brevity we have used the same method for all three case studies.

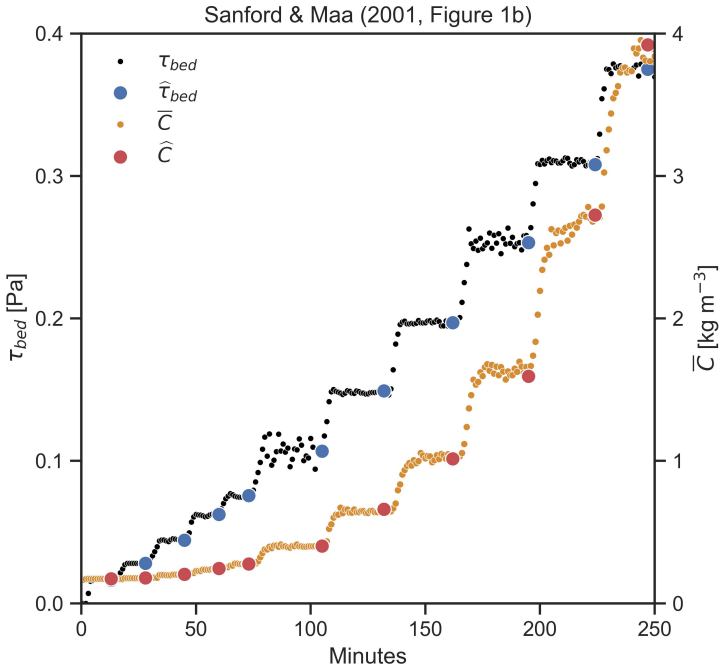

Figure 1. Observations from the Maa et al. (1998) (digitised from Sanford and Maa (2001), Figure 1b) annular flume experiment for site White Rocks showing measured bed stress and $\overline{C}$ over a period of 250 minutes. The steady state values ($\widehat{\tau}_b$ and $\widehat{C}$) used to estimate the bed strength profile are shown as the larger scatter points. $\overline{C}$ has been converted to a mass concentration (from mass per unit of bed area) for comparison with the model output.

4.2.2 Model specification

We digitised the time series of bed stress and $\overline{C}$ from Sanford and Maa (2001) and used these to estimate the numerical model parameters. The digitised data was (nearest neighbour) interpolated onto a time grid with resolution, Δ_z, of 60 seconds. The vertical grid was divided into four equal cells and the initial $\overline{C}$ was set to the observed concentration at $t = 0$. Deposition was set to zero for the entire simulation, a common assumption for cohesive sediment erosion events, thus $\partial\overline{C}/\partial t = E$. Therefore, in this case study we only estimated the parameters in the boundary flux (erosion) model, E, and not w_s. We still present w_s in the results to show that the posterior of w_s did not significantly change from its prior, because any value proposed for w_s gave the same model outcome). We implemented both erosion models, *E1* (Equation 6) and *E2* (Equation 7). The priors used for each scenario were unchanged from those specified previously. The likelihood (Equation 3) was modified to use $\overline{C}$ by taking the depth-average of the model output for each time step before evaluation.

4.2.3 Results and discussion

Scenarios *E1* and *E2* were both sampled for 25,000 iterations using 12 chains. The first 5,000 iterations of each chain were discarded as burn-in samples. Chain auto-correlation and $\widehat{R}$ convergence analysis indicated the chains were suitable for inference (not shown).

The posterior distribution for each parameter was approximated as a kernel density estimate histogram of all the accepted samples in the 12 chains (240,000 samples) [Figures 2 and 3]. The median and 95% CI of the posterior were calculated for each pa-

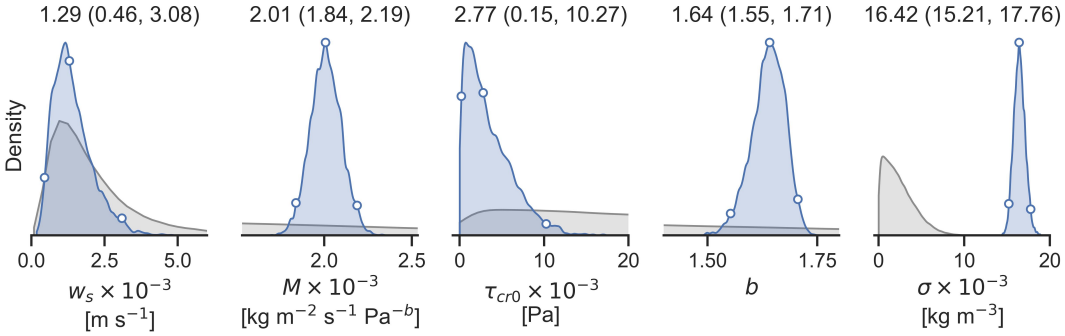

Figure 2. Posterior distributions (blue) for Case Study 1 - scenario *E1*. Prior distributions (gray) are shown over the range of the posterior, except for σ, where the range was extended to show both complete distributions. The median and lower and upper 95% CI (brackets) are shown in the axis titles and white dots on the posteriors. Note the prior distribution density may be difficult to see (close to zero) when the posterior is much more narrow than the prior.

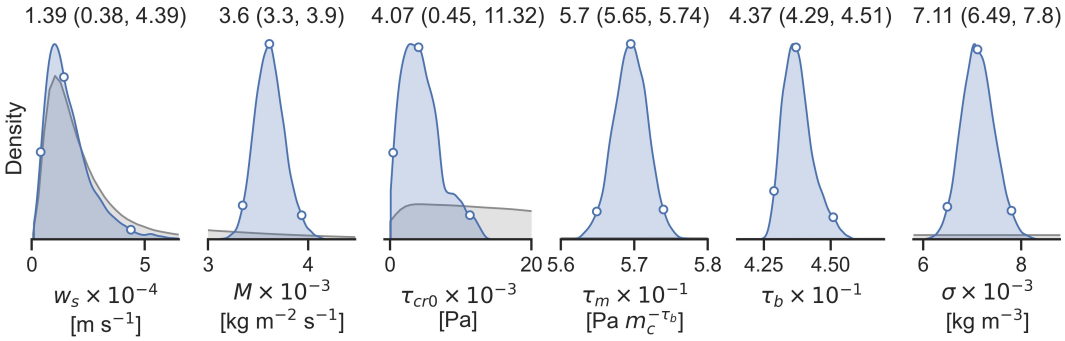

Figure 3. Posterior distributions (blue) for Case Study 1 - scenario *E2*. Prior distributions (gray) are shown over the range of the posterior. The median and lower and upper 95% CI (brackets) are shown in the axis titles and white dots on the posteriors.

rameter. Each prior distribution was sampled the same number of times for comparison. For both scenarios ($E1$ & $E2$) the posterior distributions were found to be well within the limits of the prior distributions, except for σ in *E1*, which was much higher than the prior value. This implied that the erosion model in *E1* was a poor choice for modelling the observed data in this annular flume data.

We randomly selected 10,000 samples of θ from the posterior and re-ran the numerical model for each θ to generate the posterior predictive distribution. From this we estimated the 50%, 80%, and 95% CI of the predictions, and compared them to the observations for *E1* [Figure 4 left] and *E2* [Figure 5 left].

In scenario *E1* there was significant model mis-specification. The chosen erosion model was not able to replicate the observed erosion rate decay that occurred rapidly after each increase in bed stress. Instead the results generally fit "through" the stepped observations of $\overline{C}$ [Figure 4]. This meant that the residuals were larger than expected. For scenario *E2*, however, the posterior predictions fit the observations well and the estimated σ was lower, indicating a reduction in model mis-specification (i.e. *E2* is a better model than *E1*).

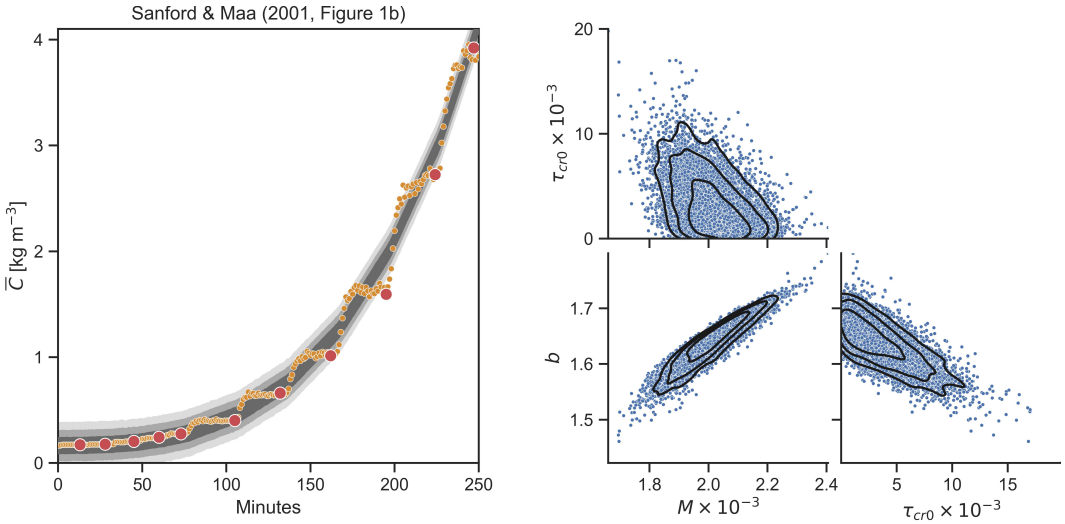

Figure 4. Left: observations of $\overline{C}$ (yellow/red) and the posterior predictive distribution of $\overline{C}$ based on 10,000 samples of the posterior for scenario $E1$. The 50%, 80%, and 95% CI of the posterior predictive distribution are shown as graduated gray shading. Right: Plots of the posterior samples from scenario $E1$ for correlated parameters only ($|r^2|$>0.3). Black lines are the 50%, 80%, and 95% density contours.

Investigation of the posterior samples in scenario *E1* indicated that all the parameters used in the erosion model (Equation 6) were correlated ($|r^2|$>0.3) [Figure 4 right]. This resulted in a wide range of parameter choices that would produce a similar erosion flux. For example, a reduction in the erosion rate M could be compensated for by either an increase in τ_{cr0} or a reduction in b, or some combination of both. The posteriors of w_s and σ were not correlated with any other parameters (not shown).

The posterior samples in scenario *E2* indicated that some parameter pairs were correlated [Figure 5 right]. While the observed parameter covariance can be sampled by this method, high correlations can result in decreased efficiency of MCMC sampling. For the later case studies we still test both erosion models $E1$ and $E2$ because they are commonly used in sediment transport modelling. We note, however, that future work could investigate erosion models more suited to inverse method sampling techniques.

For scenario *E2* we used the results to show the estimated relationship between the mass eroded, m_c, and the bed strength [Figure 6]. Note that the relationship is not just a fit of the data points (shown in blue) but of the full time series of steady and unsteady data. The bed strength estimate agrees well with the data points originally used to estimate the parameter values by Sanford and Maa (2001). This demonstrates that the method used here gave equivalent results for the estimation of the bed strength parameters, while also simultaneously estimating the erosion rate parameter, M, and σ.

This example demonstrates that the method described here can be successfully employed to estimate multiple model parameters simultaneously, using unsteady data in a controlled setting. It is important to note that the full time series of observations from the experiment has contributed to the inference process, not just the steady-state points at the end of each step. In the following case studies, the same process will be performed on data sets where neither the forcing nor the concentration C reach a steady-state.

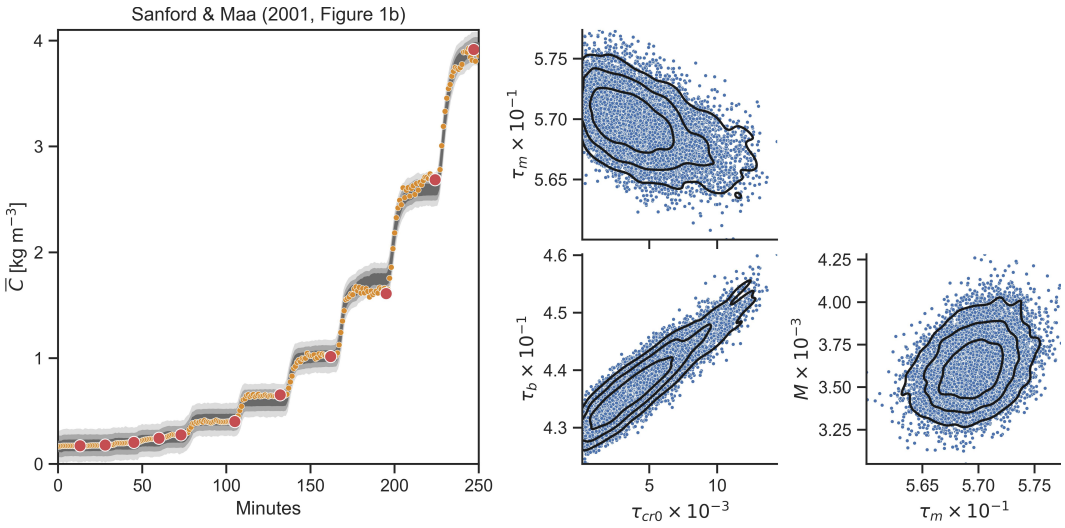

Figure 5. Left: observations of $\overline{C}$ (yellow/red) and the posterior predictive distribution of $\overline{C}$ based on 10,000 samples of the posterior for scenario $E2$. The 50%, 80%, and 95% CI of the posterior predictive distribution are shown as graduated gray shading. Right: Plots of the posterior samples from scenario $E2$ for correlated parameters only ($|r^2|$>0.3). Black lines are the 50%, 80%, and 95% density contours.

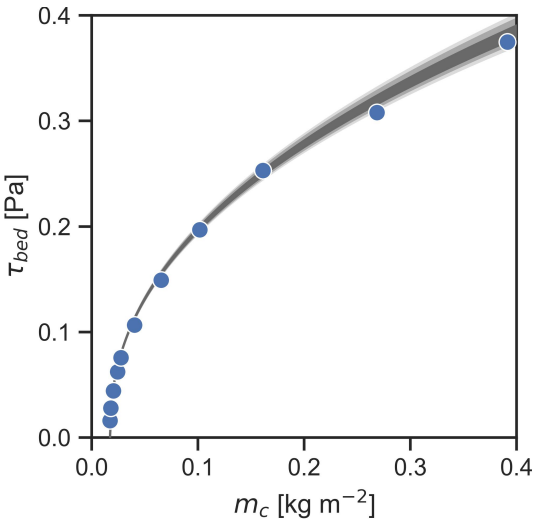

Figure 6. Total mass eroded, m_c, shown with bed strength, τ_{bed} (shown as per Sanford and Maa (2001) Figure 2a, site White Rocks). The blue dots are the applied stress and measured $\overline{C}$ values at the end of each step (as shown by the blue and red markers in Figure 1). The gray shading is the 50%, 80%, and 95% CI of the posterior predictive distribution for 10,000 samples from the bed strength parameters in erosion model $E2$ (Equation 7, τ_{cr0}, τ_m, and τ_b). Note m_c is related to $\overline{C}$ using the height of the flume.

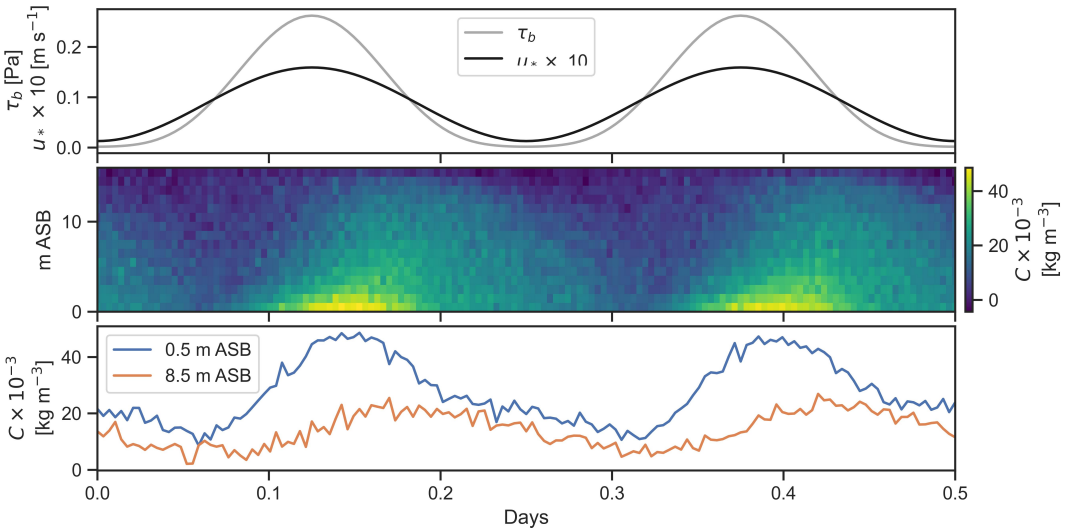

Figure 7. Top: synthetic tidal forcing data for Case Study 2, including the friction velocity, u_* (black, shown multiplied by 10), and the bed stress, τ_b (gray). Middle: filled color plot of synthetic C using erosion model *E1* (Equation 6) for the entire model grid with added Gaussian noise. Bottom: synthetic observations of C for selected heights above the bottom boundary.

4.3 Case Study 2: synthetic tidally-driven erosion

4.3.1 Observations

For this case study we generated synthetic observations with the numerical model in order to recover specified model parameters. Forcing variables were chosen to describe idealised spring tide conditions. Guided by the field observations in Edge et al. (2021), the friction velocity, u_*, was modelled as sinusoidal with a 12-hour period, thus approximating the semi-diurnal tide. The range of u_* was from 1 to 16 mm s^{-1} [Figure 7] (note the flow never comes entirely to rest in the field observations). Using the quadratic stress equation, $\tau_b = \rho u_*^2$, where ρ was 1025 kg m^{-3}, the bed stress thus varied between 0.001 and 0.262 Pa. The erosion model *E1* from Equation 6 was used to calculate the erosion flux. The underlying parameter values used to generate the synthetic observations were; $w_s = 1 \times 10^{-3}$ m s^{-1}, $M = 3 \times 10^{-4}$ kg m^{-2} s^{-1} Pa^{-b}, $\tau_{cr0} = 7 \times 10^{-2}$ Pa, and $b = 1.1$.

The model was run for one tidal cycle as a spin up, with the profile of C on the final time step used as the initial quasi-steady condition for a second run. This second run was used to generate the synthetic observations of C. We then added noise to the entire time-height grid of C in the form of random samples drawn from a Gaussian distribution with a standard deviation of 2 $\times 10^{-3}$ kg m^{-3} [Figure 7b]. Discrete observations near the bottom boundary (0.5 m ASB) and near the top of the model domain (8.5 m ASB) were extracted as the forcing observations [Figure 7 bottom]. The exact underlying standard deviation of the noise was calculated as the standard deviation of the residuals between the noisy and noise-free model observations of C ($\sigma = 0.199 \times 10^{-3}$ kg m^{-3}).

4.3.2 Model specification

The model grid was created with a vertical resolution of 1 m and a time step of 300 s. The grid resolution was chosen to be as coarse as possible while still adequately re-

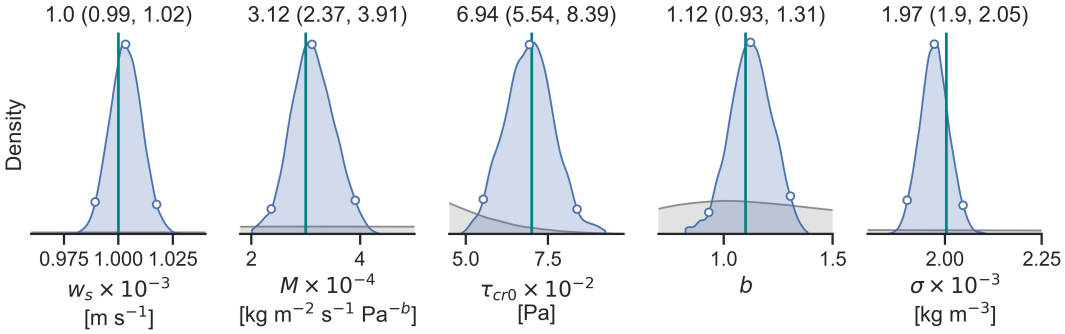

Figure 8. Posterior distributions (blue) for Case Study 2, synthetic tidally-driven erosion - scenario *E1*. Prior distributions (gray) are shown over the range of the posterior. The median and lower and upper 95% CI (brackets) are shown in the axis titles and white dots on the posteriors. The teal vertical line in each subplot was the underlying value used to generate the observations.

solving the vertical profile of C and ensuring the majority of the prior parameter space was in a region of model stability (e.g., the Courant number was generally less than one during sampling). The implicit model form provided more flexibility in this regard. The total model height was 16 m and the boundary layer height, required to calculate the eddy diffusivity profile using Equation 8, was set to a constant value of 15 m ASB. Vertical fluid velocities were set to zero for this case study.

We ran one scenario which used the erosion model *E1* in Equation 6. There was no model mis-specification in this example (the model determined the underlying observations perfectly), thereby a comparison of multiple numerical model scenarios (such as using both erosion models) was not warranted (note Case Study 2 was tested using erosion model *E2* with similar results, but was not presented for brevity). The priors used for each scenario were unchanged from those specified previously. For this example, the observations and modelled C at 0.5 and 8.5 m ASB were supplied to the likelihood function (Equation 3) as a 2D array.

The numerical model was specified with a constant deposition rate for this case. There is ongoing research into the apparent disconnect between deposition behaviour in laboratory experiments and common numerical modelling practices (see Letter and Mehta (2011) for a detailed explanation). For this work we simply note that numerical modelling of sediment transport over several tidal cycles is generally performed with a constant deposition flux. This method could be used to compare other more complex deposition models, such as Krone's probabilistic model (Winterwerp and van Kesteren (2004), Equation 5.21), a potential topic for future research.

4.3.3 Results and discussion

The scenario *E1* was sampled for 25,000 iterations using 12 chains. The first 5,000 samples were discarded as burn-in samples. Chain auto-correlation and $\widehat{R}$ convergence analysis indicated the chains were suitable for inference (not shown). The priors and posteriors were compared as per Case Study 1 [Figure 8]. The approximate form and 95% CI of the posterior was calculated for each parameter [see Figure 8 axis titles].

The inference method was able to accurately capture the underlying parameter values, with the mode and median of the posterior close to the true value [Figure 8]. The posterior distribution of w_s was narrow and the posterior samples were not correlated

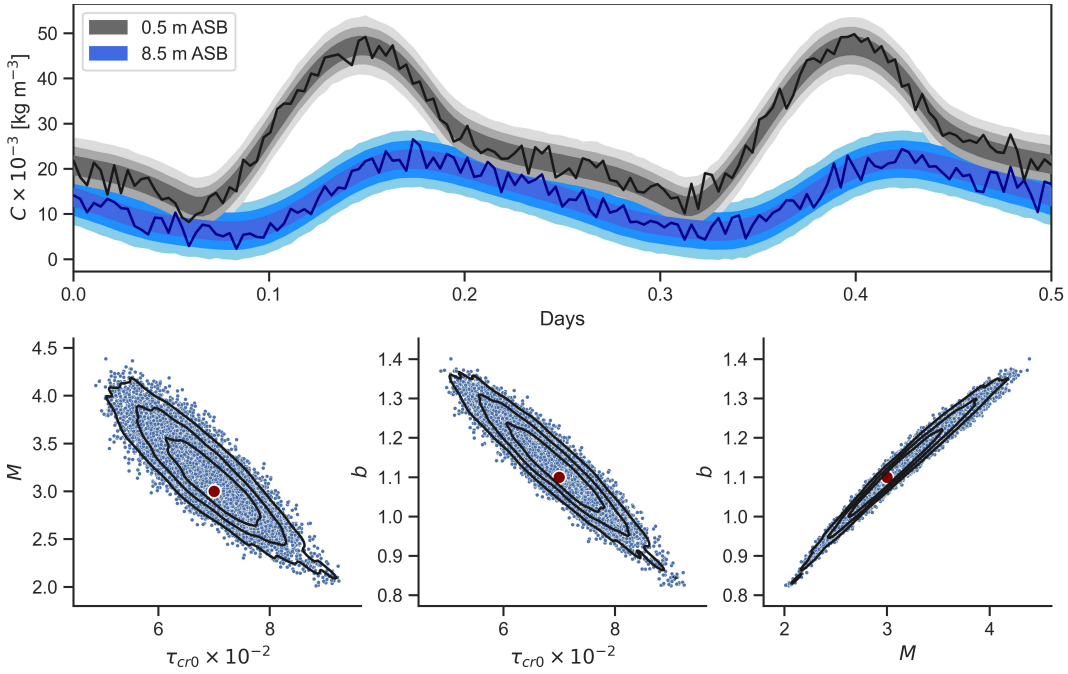

Figure 9. Top: observations of C (lines) for Case Study 2 from the two selected heights above the sea bed (ASB) and posterior predictive distributions of C at each height based on 10,000 samples of the parameter posteriors for $E1$, showing 50%, 80%, and 95% CI as graduated gray and blue shading. Bottom: Plots of posterior distribution samples of $E1$ for correlated parameters only ($|r^2|$>0.3). Maroon dots are the specified (true) parameter values. Black lines are the 50%, 80%, and 95% density contours.

with any other parameter. The posterior distributions for all of the erosion model parameters (M, τ_{cr0}, b) were wide in comparison to their median value.

We randomly selected 10,000 samples of θ from the posterior and re-ran the numerical model for each θ to generate the posterior predictive distribution. From this we estimated the 50%, 80%, and 95% CI of the predictions at the two observation heights and compared them to the noisy synthetic observations [Figure 9]. All of the erosion model parameters were correlated [Figure 9]. When estimating the posterior predictive distribution of C, however, the majority of the distribution width came from σ. This suggested that the resulting erosion flux was similar for all samples from the posterior, despite the wide posteriors.

This case study demonstrated that the method can recover the underlying specified values of the numerical model parameters even when using noisy observations. In general, the underlying parameter value was at or close to the posterior distribution median, and the erosion model posterior distributions were wide and correlated. The width of the erosion model posteriors was surprising, given the lack of model mis-specification. Testing indicated that these posteriors were more narrow and less correlated when the exponent b (Equation 6) was further from one and the erosion flux response was less linear (not shown). In cases where b is known to be approximately one this parameter could be removed from the model, thus increasing the inference efficiency. In addition, the erosion model itself could be re-parameterised to reduce parameter covariance.

459 ## 4.4 Case Study 3: Continental shelf bottom boundary observations

460 ### *4.4.1 Observations*

461 In this case study we attempt to estimate unobserved parameters using 2017 field
462 observations from the Northwest Shelf of Australia (Zulberti et al., 2022; Edge et al., 2021).
463 These studies presented data over 15 days from 2 to 16 April 2017. As it was too com-
464 putationally expensive to include the entire period in the numerical model using this method,
465 we selected a period of 3 consecutive tidal cycles (about 37.6 hours) [Figure 10]. This
466 period was chosen because it captured a range of forcing conditions and sediment response,
467 and because no large amplitude nonlinear internal waves (NLIW) propagated past the
468 site at this time; NLIW introduce strong vertical fluid velocities and are likely to cre-
469 ate horizontal gradients of C, hence creating horizontal advective effects that violate the
470 assumptions of our model. To evaluate the method, we generated predictions using in-
471 ferred posterior distributions of model parameters and compared these with independent
472 observations not used in the parameter estimation (noting that the primary purpose of
473 the method is parameter estimation and not prediction of C).

474 The friction velocity and bed stress were derived from high frequency current mea-
475 surements collected at 0.49 m ASB. Zulberti et al. (2018) showed that use of the quadratic
476 drag law with $C_D = 0.00185$ was an accurate proxy for measured Reynolds stress ($u_{*Re} =$
477 $0.99u_{*Cd} + 0.00$, $r^2 = 0.92$) within the log-layer (typically 1 m thick) at this site and
478 provided a more complete record. Eddy diffusivity profiles, γ_z, were calculated as per
479 Equation 8 with the time-varying bottom boundary layer height (BBL) (typically 10 m
480 thick) estimated using backscatter from an acoustic Doppler current profiler (ADCP),
481 as per Zulberti et al. (2022) [Figure 11]. Direct estimates of eddy diffusivity at 1.4 m ASB
482 were typically three times greater than modelled estimates using Equation 8 (the model
483 is highly idealised). Zulberti et al. (2022) analysed backscatter, current profiles and tem-
484 perature profiles, and determined that backscatter could be used as a suitable proxy to
485 estimate the BBL height. Fluid vertical velocities were supplied by the ADCP. Points
486 close to the sea bed where the ADCP returned poor vertical velocity data were linearly
487 extrapolated to zero at the bed. Both the BBL height and vertical velocities were low-
488 pass filtered.

489 The observations of C, taken from Edge et al. (2021), were chosen at two discrete
490 heights, 1.4 m and 9.5 m ASB [Figure 10, bottom]. In addition, we performed the in-
491 ference with a single point measurement (at 1.4 m ASB) in order to test the method sen-
492 sitivity and applicability to cases where only a single observation height was available.

493 Closer examination of the forcing data and observations highlights the complex be-
494 haviour of the continental shelf boundary layer during this period with both barotropic
495 and (out-of-phase) baroclinic tides influencing the currents and hence the bottom stress
496 [Figure 11]. The bed stress is not a simple sinusoid: on odd-numbered half-tides the stress
497 was intensified by internal tides that generate an additional near-bed current. For even-
498 numbered tides the opposite was true, with internal tides generating an adverse near-
499 bed current, reducing the estimated bed stress and u_*. The near-bed C exhibited var-
500 ied responses to similar magnitudes of bed stress and there was a time-lag in the response
501 at different observation heights. Note that the periods where C was greater at the higher
502 observation point were likely the result of calibration uncertainty and not a negative sed-
503 iment gradient [Figure 11, bottom] (calibration uncertainty was not included in this work,
504 but is a topic of future research).

505 ### *4.4.2 Model specification*

506 The model grid was similar to Case Study 2, with a vertical resolution of 1 m and
507 a time step of 300 s. The total model height was 24 m with the maximum BBL height
508 remaining under 20 m. We ran two different numerical model scenarios for this case study,

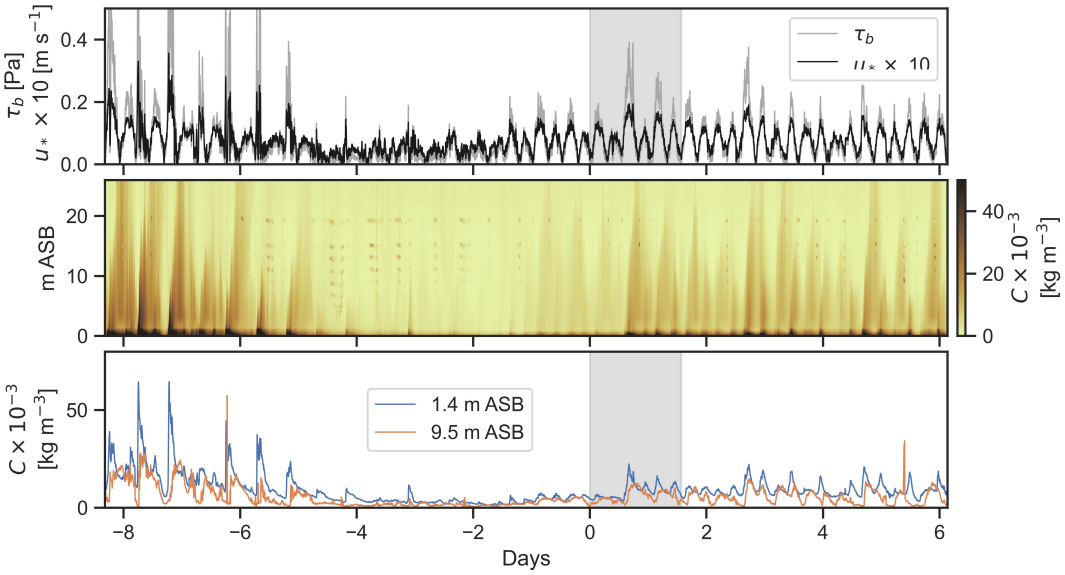

Figure 10. 15 days of oceanographic data from Zulberti et al. (2022) and Edge et al. (2021). The top panel shows the estimated bed shear stress, τ_{bed}, and friction velocity, u_*, from high frequency current measurements at 0.49 m ASB. The middle panel shows a compilation of C observations, primarily from the ADCP over the bottom 23 m ASB. The bottom panel shows the two observed time series of C used for Case Study 3. The gray shaded area shows the three tidal cycle periods used in Case Study 3.

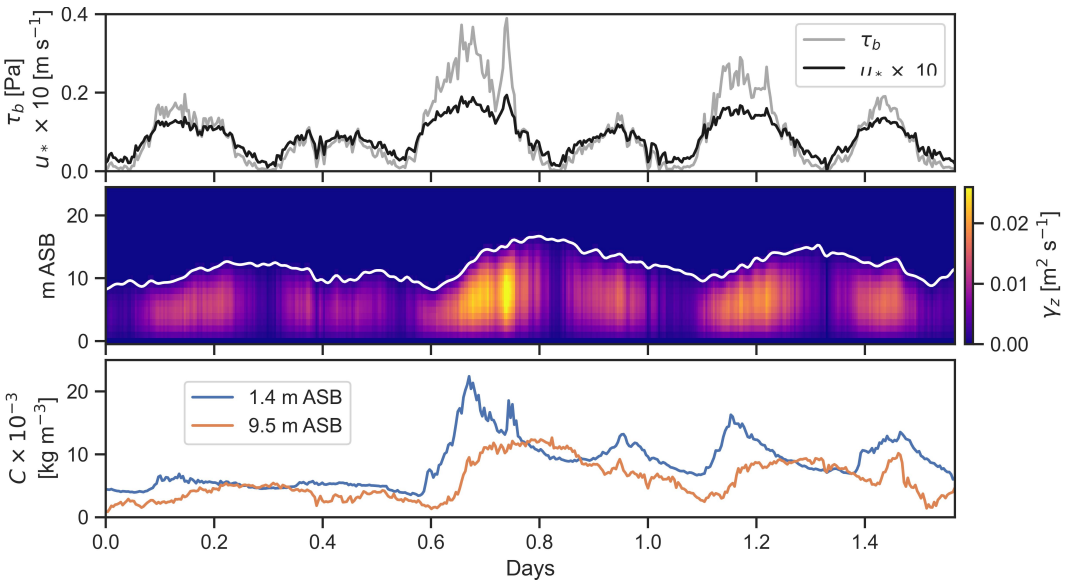

Figure 11. Forcing data and observations of C for Case Study 3. The top panel shows the measured bed stress and friction velocity at the bed. The middle panel shows the eddy diffusivity and the low-pass filtered BBL height (white line). The bottom panel shows the observations of C used for this case study.

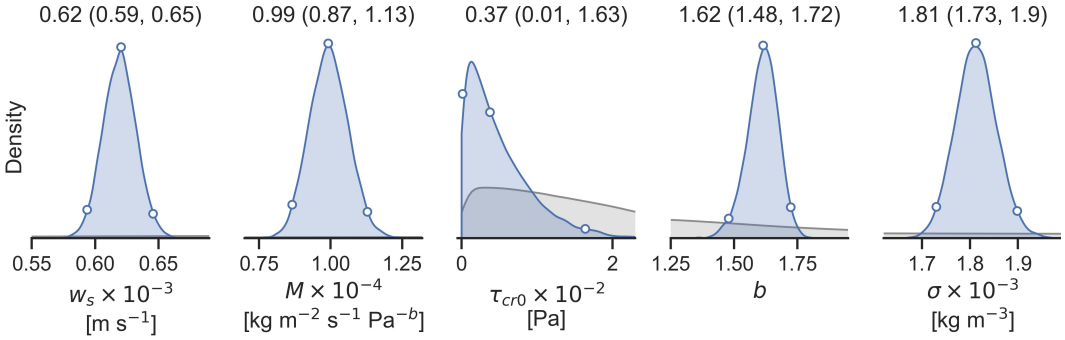

Figure 12. Posterior distributions (blue) for Case Study 3 - scenario *E1*. Prior distributions (gray) are shown over the range of the posterior. The median and lower and upper 95% CI (brackets) are shown in the axis titles and white dots on the posteriors.

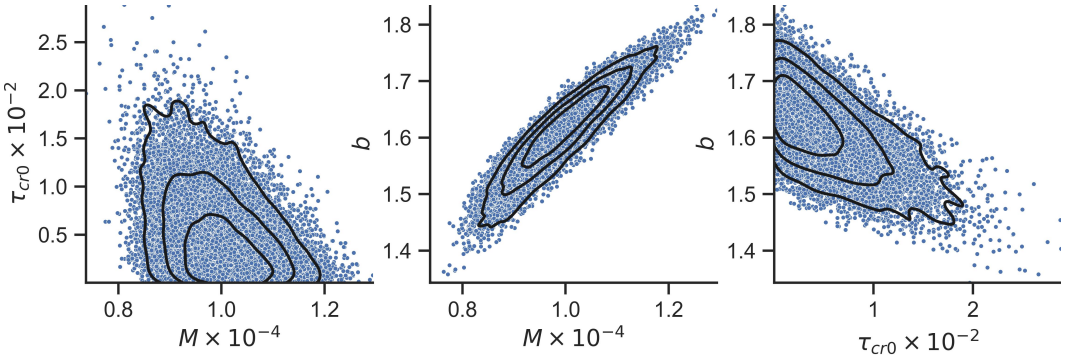

Figure 13. Posterior distribution samples for Case Study 3 - scenario *E1* for the correlated parameters only ($|r^2|$>0.3). Black lines are the 50%, 80%, and 95% density contours.

E1 using the erosion model in Equation 6, and *E2* using the erosion model in Equation 7. The priors used for each scenario were unchanged from those specified previously. In addition, a modified scenario was also assessed based on scenario *E2* that only used observations from a single height at 1.4 m ASB, rather than two heights (denoted *E2-1obs*). Note the numerical model output was interpolated (quadratic) to estimate C at 1.4 m, as the grid points were spaced at 1 m intervals starting at 0.5 m.

4.5 Results and discussion

All three scenarios ($E1$, $E2$, and *E2-1obs*) were sampled for 25,000 iterations using 12 chains. The first 5,000 iterations of each chain were discarded as burn-in samples. Chain auto-correlation and $\widehat{R}$ convergence analysis indicated the chains were suitable for inference (not shown). Kernel density estimates were used to visually compare the prior and posterior distributions for scenario $E1$ [Figure 12]. Parameters M, τ_{cr0}, and b were correlated ($|r^2|$>0.3) in scenario $E1$ [Figure 13], similar to the previous case studies. Parameter estimates from the $E2$ and *E2-1obs* scenario variations were compared visually using kernel density estimates [Figure 14] and several of the parameters were positively correlated (r^2>0.3) [Figure 15].

Scenarios $E1$ and $E2$ provided similar estimates for comparable parameters (w_s, M, τ_{cr0}, and σ). The settling velocity, w_s, was estimated to be around 0.16 $\times$ 10^{-4} m s^{-1} slower in $E2$ compared to $E1$. Mean particle size and effective density measurements from Edge et al. (2021) gave an estimated mean w_s of 0.6 $\times$ 10^{-4} m s^{-1} using Stokes'

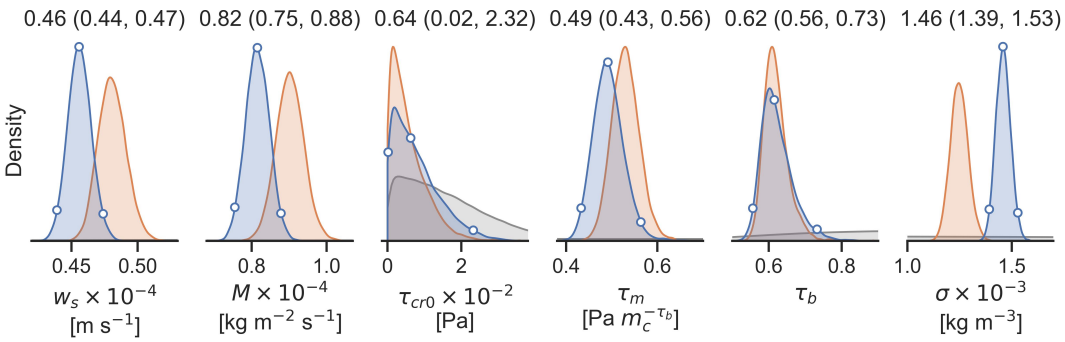

Figure 14. Posterior distributions for Case Study 3 - scenario *E2* (blue) and scenario *E2-1obs* (orange). Prior distributions (gray) are shown over the range of the posteriors. The median and lower and upper 95% CI (brackets) are shown for only scenario *E2* in the axis titles and white dots on the posteriors.

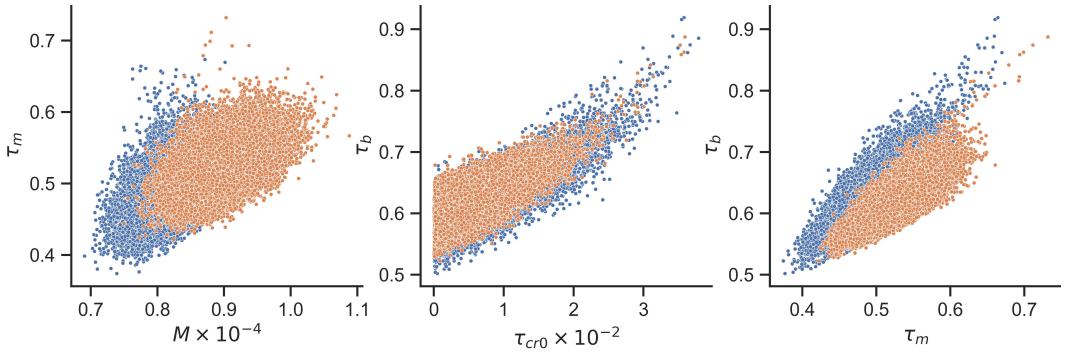

Figure 15. Posterior distribution samples for Case Study 3 - scenario *E2* (blue) and scenario *E2-1obs* (orange) for the correlated parameters only ($|r^2|$>0.3, shown without contours for clarity).

law. Posterior distributions of the initial bed strength (critical shear stress), τ_{cr0}, could be approximated by a half-normal distribution shape in both scenarios. The observations do not contain significant time periods where τ_{bed} was in the range of τ_{cr0} and so the likelihood function was insensitive to changes in τ_{cr0} at small values. The posterior predictions were narrower for scenario $E2$, compared to $E1$ [Figure 16], indicating a better fit using the $E2$ erosion model.

The two variations of scenario *E2* (*E2* and *E2-1obs*) provided interesting insight into how much data was needed to infer the parameters and how changing the input observations affected σ [Figure 14]. Notably, the inferred parameters were both in a similar range, which suggested the method was (relatively) insensitive to the chosen height of measurements of C. Using observations from only a single height in scenario *E2-1obs* also shifted the posterior distribution for some parameters [Figure 14].

We did not expect the results for scenarios *E2* and *E2-1obs* to be similar as the use of observations at a single point could in theory be matched with many values of w_s (and hence profiles of C). It appeared, however, that the information contained within the time series of C at a single point was sufficient to infer the model parameters, noting that the prior distributions help inform the estimate. In addition, using less observations reduced σ, indicating that the erosion model in scenario $E2-2obs$ could better represent the time series of C close to the bottom boundary (compared to C further from the bed). Note that the distributions of σ for scenarios *E2* and *E2-1obs* were not directly comparable as the observation data sets were different (Scenario *E2-1obs* used less data points).

We compared the observations to posterior predictive distributions of C using 10,000 randomly selected samples from θ. The 50%, 80%, and 95% CI of the predictions were calculated at the two observation heights above the sea bed (1.4 m and 9.5 m). The results were similar for all three scenarios, so only predictions for scenarios *E1* and *E2* are presented [Figure 16 top and bottom, respectively].

To demonstrate the ability of the model to make predictions beyond the chosen inference period, we extended the model run. We supplied the forcing data; bed stress, bottom friction velocity, vertical velocity, and BBL height, to the model for the extended period. We then generated posterior predictive samples for this period using the scenario *E2-1obs* and calculated the 50%, 80%, and 95% CI at 1.4 m and 9.5 m ASB [Figure 17]. While this scenario did not use any observations of C at 9.5 m for the inference, it still made good predictions at this height for the original model period. Beyond the original model period the predictions and observations diverged at both heights.

It is clear from the results with the Case Study 3 field observations, that in addition to natural variation and measurement errors, in both erosion model scenarios there is missing physics, as reflected in σ. The primary sources of model mis-specification are likely to come from simplification of the ADE and the boundary flux models used (i.e. the erosion and deposition models). Simplification of the ADE for this model may have discounted potentially important horizontal advection processes, such as horizontal sediment gradients induced by the internal tide. Improvement of the boundary flux models is a common aim for sediment transport studies and this method shows promise in quantifying relative model performance. Future work could also include the implementation of a multi-layer bed model with consolidation and multiple sediment size classes.

5 Conclusions

We have demonstrated that MCMC sampling can be used in conjunction with a simple 1D advection-diffusion numerical model (including its boundary model) to estimate parameters of interest with uncertainty quantification. The numerical model itself used a well known discretisation method and has the potential for inclusion of any bound-

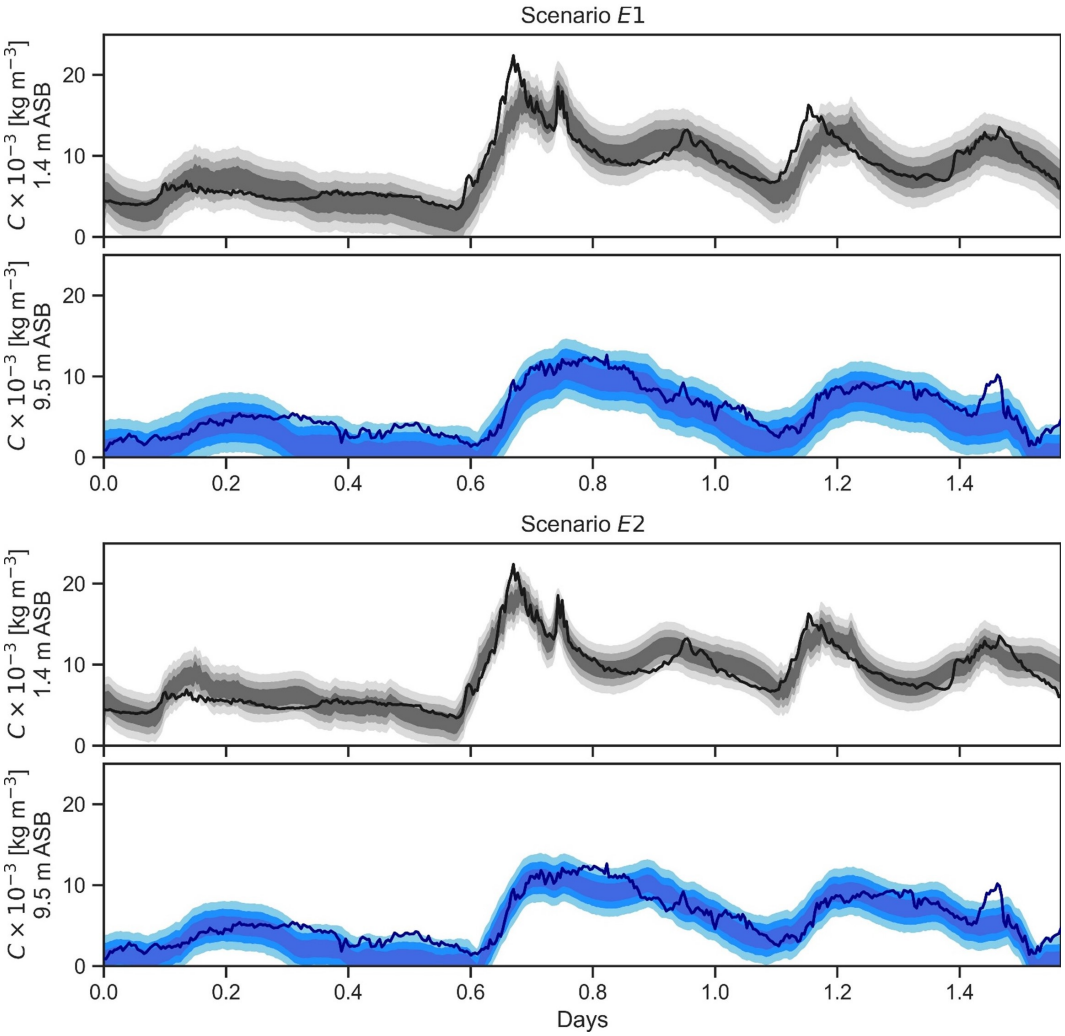

Figure 16. Top plots: Case Study 3 observations of C (solid lines) and the 50%, 80%, and 95% CI of the posterior predictive distributions of C from Scenario $E1$ (graduated shading) at 1.4 m above the sea bed (ASB) (gray) and 9.5 m ASB (blue). Bottom plots: as per the top plots for Scenario $E2$.

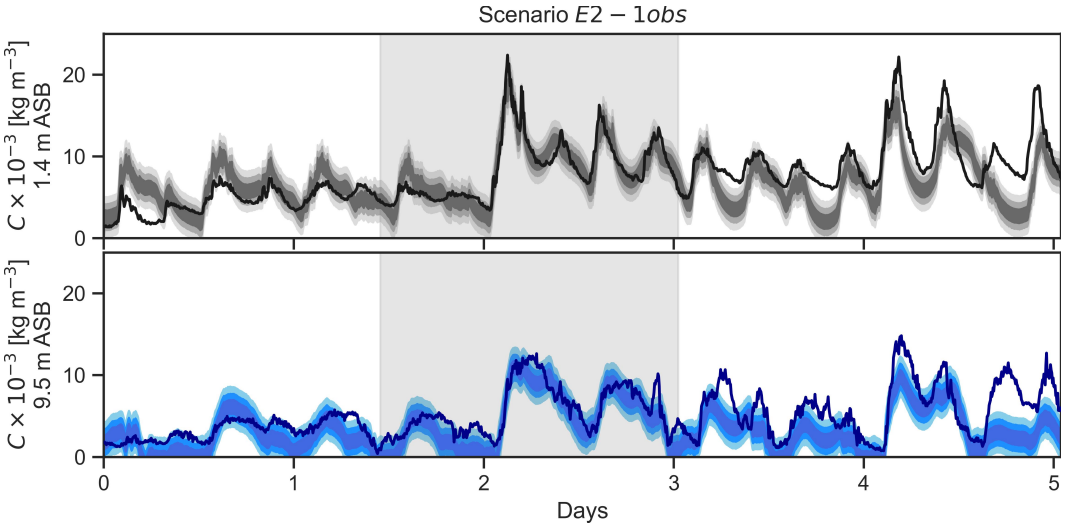

Figure 17. Top: Case Study 3 - scenario *E2-1obs* extended observations of C (solid line) at 1.4 m above the sea bed (ASB) and 50%, 80%, and 95% CI of the posterior predictive distributions of C (graduated gray shading). Bottom: as per top panel but for C at 9.5 m ASB (blue line and shading). The original model period is shown as light gray shading in both plots.

ary model (in this case erosion or deposition). This allows for a quantitative comparison of the performance of any model selected from literature as applied to a given data set of observations.

We have applied this method to three case studies from the field of cohesive sediment transport. Case Study 1 was an example of a common erosion test conducted using an in-situ annular flume. In this scenario, the depth-averaged C was supplied which simplified the analysis. We demonstrated that the entire time series of bed stress and C could be used to infer model parameters, where previously only steady state periods have been used. This indicates that the method should be suitable to apply to similar investigations with unsteady forcing, such as channel or estuary flows. In-situ parameter estimation in cohesive sediment environments such as these is a difficult task, with conflicting results between methods (e.g. Maa & Kwon, 2007), and state-of-the-art measurement techniques giving a wide range of (potentially noisy) estimates (e.g. Egan et al., 2021).

We then applied the method to Case studies 2 and 3, synthetic and real examples of complex BBL forcing and response on the continental shelf. These observations motivated this work due to the difficulty of measuring the inferred parameters directly in deep environments (the development and testing of new in-situ measurement techniques is better suited to shallow environments such as channels and estuaries). Using the method described in this paper we were able to infer quantitative information on difficult to observe parameters using measurements that are simple to collect (current velocity and suspended sediment concentration from acoustic backscatter). We note that this simple coarse resolution model still required computation time of around 2 days (Intel(R) Core(TM) i7-7700 CPU @ 3.60GHz), so the method may be too computationally costly to apply to 2- and 3-dimensional numerical models (note there is much literature available on other methods for larger models (e.g. Bui-Thanh et al., 2012)).

The key output from this method was the posterior distributions of each parameter, with predictions being a secondary outcome. Nevertheless, posterior predictions of C were in agreement with observations (as they must be to achieve good results) but ex-

tended predictions diverged from observations outside the original inference period. This was likely due to the simplified representation of baroclinic tides in the model, which, in reality, were not phase-locked with the barotropic tide. The divergence in predictions may also be due to changes in the key parameters with time or some other aspect of model mis-specification.

In summary, the method described here was able to infer key model parameters with uncertainty. The method inherently partitions uncertainty from the parameters and the model mis-specification and the measurement error term (σ). A more sophisticated model (e.g., a discretized bed model or a more realistic diffusivity model) could readily be implemented to potentially improve the results. Furthermore, we expect this method would perform even better if applied to a less complex system, such as a shallow tidal channel.

6 Open Research

Forcing and fitting data used for Case Study 3 are archived on two UWA library research data repositories (Zulberti et al., 2020; Edge, 2021). No proprietary software has been used for this research. All analysis was conducted using Python 3 with the exception of exporting raw instrument data using manufacturer's software. Specific packages utilised frequently for this work (although not specifically required) include *Pymc*3 (Salvatier et al., 2016), *Seaborn* (Waskom, 2021), *Xarray* (Hoyer & Hamman, 2017), and any packages they depend on. Jupyter Notebooks can be supplied upon request.

Acknowledgments

We thank Andrew Zulberti for the provision of processed ADV and ADCP data used in this work. This work was funded by the Australian Research Council (ARC) Research Training Program scholarship, the ARC Industrial Transformation Research Hub for Offshore Floating Facilities (IH140100012), and an ARC Discovery Grant (DP140101322).

References

Ariathurai, C. R. (1974). *A finite element model for sediment transport in estuaries* (Unpublished doctoral dissertation). University of California, Davis.

Brand, A., Lacy, J. R., Gladding, S., Holleman, R., & Stacey, M. (2015). Model-based interpretation of sediment concentration and vertical flux measurements in a shallow estuarine environment. *Limnology and Oceanography*, *60*(2), 463–481. doi: 10.1002/lno.10047

Bui-Thanh, T., Burstedde, C., Ghattas, O., Martin, J., Stadler, G., & Wilcox, L. (2012). Extreme-scale uq for bayesian inverse problems governed by pdes. *Proceedings of the International Conference on High Performance Computing, Networking, Storage and Analysis*, 3:1-3:11.

Cartwright, G. M., Friedrichs, C. T., & Smith, S. J. (2013). A test of the ADV-based Reynolds flux method for in situ estimation of sediment settling velocity in a muddy estuary. *Geo-Marine Letters*, *33*(6), 477–484. doi: 10.1007/s00367-013-0340-4

Dyer, K. R., & Soulsby, R. L. (1988). Sand transport on the continental shelf. *Ann. Rev. Fluid Mech., 20 , 1988*, 295–324. doi: 10.1146/annurev.fl.20.010188.001455

Edge, W. C. (2021). *Bottom boundary-layer and profiling sediment observations beneath nliw* [dataset]. The University of Western Australia. doi: 10.26182/hyw0-my35

Edge, W. C., Jones, N. L., Rayson, M. D., & Ivey, G. N. (2021). Calibrated Suspended Sediment Observations Beneath Large Amplitude Non-Linear Inter-

nal Waves. *Journal of Geophysical Research: Oceans*, *126*(12), 1–27. doi: 10.1029/2021JC017538

Egan, G., Chang, G., McWilliams, S., Revelas, G., Fringer, O. B., Monismith, S. G., ... Monismith, S. G. (2021). Cohesive Sediment Erosion in a Combined Wave-Current Boundary Layer. *Journal of Geophysical Research: Oceans*, *126*(2), 1–17. doi: 10.1029/2020JC016655

Gelman, A., Carlin, J., Stern, H., Dunson, D., Vehtari, A., & Rubin, D. (2013). *Bayesian data analysis* (3rd ed.). CRC Press.

Ghouili, N., Ribeiro, L., Zammouri, M., & Horriche, F. J. (2017). Effect of the spatial variability of transmissivity on the groundwater flow and budget of the Takelsa multilayer aquifer, Tunisia. *Environmental Earth Sciences*, *76*(20), 1–18. doi: 10.1007/s12665-017-7021-y

Hoyer, S., & Hamman, J. (2017). xarray: N-D labeled arrays and datasets in Python. *Journal of Open Research Software*, *5*(1). doi: 10.5334/jors.148

Letter, J. V., & Mehta, A. J. (2011). A heuristic examination of cohesive sediment bed exchange in turbulent flows. *Coastal Engineering*, *58*(8), 779–789. doi: 10.1016/j.coastaleng.2011.04.003

Liñán Baena, C., Andreo, B., Mudry, J., & Carrasco Cantos, F. (2009). Groundwater temperature and electrical conductivity as tools to characterize flow patterns in carbonate aquifers: The Sierra de las Nieves karst aquifer, southern Spain. *Hydrogeology Journal*, *17*(4), 843–853. doi: 10.1007/s10040-008-0395-x

Maa, J. P., & Kwon, J. I. (2007). Using ADV for cohesive sediment settling velocity measurements. *Estuarine, Coastal and Shelf Science*, *73*(1-2), 351–354. doi: 10.1016/j.ecss.2007.01.008

Maa, J. P., Sanford, L., & Halka, J. P. (1998). Sediment resuspension characteristics in Baltimore Harbor, Maryland. *Marine Geology*, *146*(1-4), 137–145. doi: 10.1016/S0025-3227(97)00120-5

Manning, A. J., & Schoellhamer, D. H. (2013). Factors controlling floc settling velocity along a longitudinal estuarine transect. *Marine Geology*, *345*, 266–280. doi: 10.1016/j.margeo.2013.06.018

Mattsson, J., Mattsson, A., Davidsson, F., Hedström, A., Österlund, H., & Viklander, M. (2016). Normalization of Wastewater Quality to Estimate Infiltration/Inflow and Mass Flows of Metals. *Journal of Environmental Engineering*, *142*(11), 04016050. doi: 10.1061/(asce)ee.1943-7870.0001120

Neville, B. T. (1986). Field settling velocities of estuary muds. *Estuarine Cohesive Sediment Dynamics: Proceedings of a Workshop on Cohesive Sediment Dynamics with Special Reference to Physical Processes in Estuaries, Tampa, Florida, November 12–14, 1984*, 126–150. doi: 10.1007/978-1-4612-4936-8

Păun, L. M., Qureshi, M. U., Colebank, M., Hill, N. A., Olufsen, M. S., Haider, M. A., & Husmeier, D. (2018). MCMC methods for inference in a mathematical model of pulmonary circulation. *Statistica Neerlandica*, *72*(3), 306–338. doi: 10.1111/stan.12132

Salvatier, J., Wiecki, T. V., & Fonnesbeck, C. (2016). Probabilistic programming in python using pymc3. *PeerJ Comput. Sci.*, *2*, e55.

Sanford, L. P. (2008). Modeling a dynamically varying mixed sediment bed with erosion, deposition, bioturbation, consolidation, and armoring. *Computers and Geosciences*, *34*(10), 1263–1283. doi: 10.1016/j.cageo.2008.02.011

Sanford, L. P., & Maa, J. P. (2001). A unified erosion formulation for fine sediments. *Marine Geology*, *179*(1-2), 9–23. doi: 10.1016/S0025-3227(01)00201-8

Schmelter, M. L., Hooten, M. B., & Stevens, D. K. (2011). Bayesian sediment transport model for unisize bed load. *Water Resources Research*, *47*, 1-15. doi: 10.1029/2011WR010754

Smyth, W. D., Warner, S. J., Moum, J. N., Pham, H., & Sarkar, S. (2021). What controls the deep cycle? Proxies for equatorial turbulence. *Journal of Physical Oceanography*, 2291–2302. doi: 10.1175/jpo-d-20-0236.1

Soubeyrand, S., & Roques, L. (2014). Parameter estimation for reaction-diffusion models of biological invasions. *Population Ecology*, *56*(2), 427–434. doi: 10.1007/s10144-013-0415-0

Souza, A. N., Wagner, G. L., Ramadhan, A., Allen, B., Churavy, V., Schloss, J., ... Ferrari, R. (2020). Uncertainty quantification of ocean parameterizations: Application to the k-profile-parameterization for penetrative convection. *Journal of Advances in Modeling Earth Systems*, *12*(12). doi: https://doi.org/10.1029/2020MS002108

Speagle, J. S. (2020). DYNESTY: a dynamic nested sampling package for estimating Bayesian posteriors and evidences. *Monthly Notices of the Royal Astronomical Society*, *493*(3), 3132–3158. doi: 10.1093/MNRAS/STAA278

Tarantola, A. (2004). *Inverse problem theory and methods for model parameter estimation*. USA: Society for Industrial and Applied Mathematics.

Ter Braak, C. J. (2006). A Markov Chain Monte Carlo version of the genetic algorithm Differential Evolution: Easy Bayesian computing for real parameter spaces. *Statistics and Computing*, *16*(3), 239–249. doi: 10.1007/s11222-006-8769-1

Valipour, R., Boegman, L., Bouffard, D., & Rao, Y. R. (2017). Sediment resuspension mechanisms and their contributions to high-turbidity events in a large lake. *Limnology and Oceanography*, *62*(3), 1045–1065. doi: 10.1002/lno.10485

Voulgaris, G., & Meyers, S. T. (2004). Temporal variability of hydrodynamics, sediment concentration and sediment settling velocity in a tidal creek. *Continental Shelf Research*, *24*(15), 1659–1683. doi: 10.1016/j.csr.2004.05.006

Waskom, M. L. (2021). seaborn: statistical data visualization. *Journal of Open Source Software*, *6*(60), 3021. doi: 10.21105/joss.03021

Winterwerp, J. C., & van Kesteren, W. G. M. (2004). *Introduction to the physics of cohesive sediment in the marine environment* (Vol. Developments in Sedimentology). Elsevier.

Zhang, S., Nielsen, P., Perrochet, P., Xu, B., Jia, Y., & Wen, M. (2021). Derivation of settling velocity, eddy diffusivity and pick-up rate from field-measured suspended sediment concentration profiles in the horizontally uniform but vertically unsteady scenario. *Applied Ocean Research*, *107*. doi: 10.1016/j.apor.2020.102485

Zulberti, A. P., Ivey, G. N., & Jones, N. L. (2018). Observations of Near-bed Stress beneath Nonlinear Internal Wave Trains in the Ocean. In *21st australasian fluid mechanics conference* (pp. 13–16).

Zulberti, A. P., Jones, N. L., & Ivey, G. N. (2020). *Bottom boundary-layer observations beneath nliw of depression; april 3* [dataset]. The University of Western Australia. doi: 10.26182/5f62f6e361872

Zulberti, A. P., Jones, N. L., Rayson, M. D., & Ivey, G. N. (2022). Mean and Turbulent Characteristics of a Bottom Mixing-Layer Forced by a Strong Surface Tide and Large Amplitude Internal Waves. *Journal of Geophysical Research: Oceans*, *127*(1). doi: 10.1029/2020JC017055